CHEMISTRY OF MATERIALS

pubs.acs.org/cm

Article

Open Access

This article is licensed under CC-BY 4.0

Engineering the Artificial Cathode-Electrolyte Interphase Coating for Solid-State Batteries via Tailored Annealing

Maximilian Kissel, Felix Walther, Jonas Hertle, Thomas Demuth, Ruizhuo Zhang, Philipp Brüner, Torsten Brezesinski, Kerstin Volz, and Jürgen Janek*

Cite This: *Chem. Mater.* 2025, 37, 2192–2203

Read Online

ACCESS | Metrics & More | Article Recommendations | Supporting Information

ABSTRACT: Solid-state batteries with nickel-rich layered oxide cathode active materials (CAMs) and sulfide-based solid electrolytes (SEs) are emerging as promising candidates for next-generation energy-storage systems. However, both active and electrolyte materials suffer from poor (electro)chemical compatibility, leading to severe degradation at the SE|CAM interface which is highly detrimental to the long-term cycling stability. Inspired by the natural cathode-electrolyte interphase (CEI), a novel coating concept involves formation of a protective, artificial CEI coating prior to cell assembly. Here, we investigate the oxidative annealing process after coating Li_3PS_4 as precursor onto polycrystalline $LiNi_{0.85}Co_{0.10}Mn_{0.05}O_2$ (NCM85). A combination of microscopic (scanning transmission electron microscopy, STEM), spectroscopic/spectrometric (X-ray photoelectron spectroscopy, XPS, low energy ion scattering, LEIS, and time-of-flight secondary ion mass spectrometry, ToF-SIMS), and electrochemical methods reveals that the composition, morphology, and performance of the coating can be tailored by controlled annealing in oxidizing atmosphere. The effect on coating quality and its stabilizing effect on the SE|CAM interface are examined. Only a morphologically and compositionally optimized coating can successfully prevent interfacial degradation, highlighting the need for tailored process parameters to fully exploit the coating potential. The optimization is supported by an efficient benchmarking framework combining electrochemical and analytical methods, which can serve as a basis for further systematic coating studies.

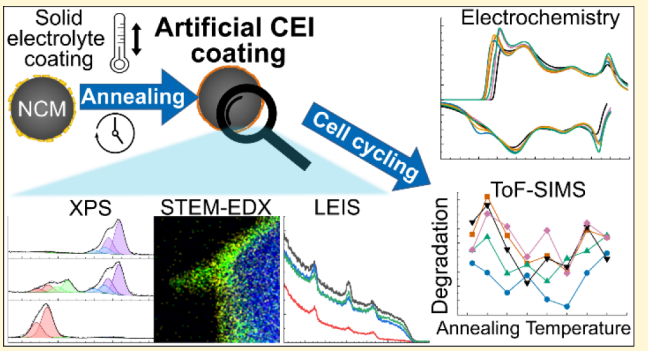

Downloaded via KIT BIBLIOTHEK on April 22, 2025 at 10:21:00 (UTC).
See https://pubs.acs.org/sharingguidelines for options on how to legitimately share published articles.

INTRODUCTION

Solid-state batteries (SSBs) are considered promising candidates for next-generation energy storage, mainly due to their potential for higher energy density and potentially improved safety compared to conventional lithium-ion batteries (LIBs).[1−5] Achieving very high energy densities requires the use of a Li-metal anode, which is assumed to be enabled by a solid electrolyte (SE) separator.[6,7] Besides, silicon has recently gained attention as anode material in LIBs and lithium-ion SSBs due to its high specific capacity and low potential of 0.4 V vs Li^+/Li.[8,9] The anode in SSBs is separated by an (ideally) dense and thin SE layer from the cathode to prevent any chemical crossover between the electrodes and to provide electronic insulation. The cathode is typically a composite consisting of SE particles (often called catholyte), cathode active material (CAM) and may also contain an electron-conducting additive and a binder. With regard to materials in the cathode composite, various combinations of CAMs and SEs have been intensely explored.[10] As CAMs, Ni-rich $LiNi_xCo_yMn1_{-x-y}O_2$ (NCM) layered oxides are currently favored, while research on $LiFePO_4$ (LFP)-based SSBs is scarce.[11−14] Ni-rich CAMs are particularly promising, since they offer high theoretical specific capacities and high operating voltages, small volume change upon delithiation/lithiation, as well as being less resource-critical than e.g., $LiCoO_2$ (LCO).[15] Different types of SEs have been tested as catholytes, such as sulfides, oxides, polymers, halides, or composite/hybrid SEs.[16−19] Recently, even the incorporation of a small amount of liquid electrolyte has been regarded as a feasible approach, which may be considered as a route from all-solid to "almost-solid".[20,21] While each SE class has distinct advantages and disadvantages, sulfide SEs are of particular interest as catholytes, since they offer very high ionic conductivities, exceeding 10 mS/cm at room temperature, as recently achieved by high-entropy SEs for example.[22,23] Another advantage is their deformability and processability, eliminating the need for energy-, time-, and cost-intensive

Received: November 7, 2024
Revised: March 5, 2025
Accepted: March 6, 2025
Published: March 11, 2025

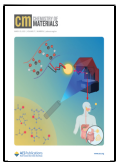

© 2025 The Authors. Published by American Chemical Society

sintering processes, which otherwise can also lead to the formation of unwanted phases.[24]

However, a critical challenge in implementing sulfide SEs and Ni-rich CAMs are interfacial degradation processes caused by the chemical and electrochemical incompatibility of the materials used.[25−28] As previously reported, this interfacial degradation is especially severe at high states of charge,[29] resulting in damage to both the SE and CAM and the formation of unwanted interfacial side products (i.e., an interphase) within a cathode-electrolyte interphase (CEI).[30] The CEI—as well as any structurally degraded near-surface layer in the NCM—impedes Li-ion transport, increases interfacial resistance, and ultimately degrades the cell performance. It is generally composed of two major types of oxidized degradation products: Polysulfides formed by electrochemical oxidation (delithiation) of the SE[31,32] and oxygenated sulfurous and phosphorous species, formed by oxygen-involving oxidation.[33,34] The latter is supposed to be more detrimental to cell degradation.[35] The required oxygen is released from the NCM lattice, reacts with the SE, thereby forming oxygenated sulfurous species (sulfites/sulfates, Li_xSO_y), oxygenated phosphorous species (phosphites/phosphates, Li_xPO_y), and mixed phases of type $Li_xP_yS_zO_u$.[36] In addition, gaseous reaction products like SO_2 have been reported.[37,38] The oxygen loss from the NCM particles causes surface reconstruction with rock-salt-phase formation, which is well-known to block Li-ion transport.[30,36] In addition to the (electro)chemical reactions, the NCM particles undergo morphological and chemo-mechanical degradation. Cycling-induced volume expansion and contraction cause cracking of CAM particles and contact loss between SE/CAM and CAM/CAM, resulting in an increased overpotential and reduced attainable capacity.[39]

In order to prevent the aforementioned degradation phenomena, various CAM coatings have been investigated.[40] The idea is that a thin layer of material on the CAM surface acts as a physical and/or chemical barrier, hindering interfacial reactions between CAM and SE.[41,42] Different approaches have been explored, including the application of ternary lithium oxides, with $LiNbO_3$ being a prominent example,[43] binary oxides (e.g., HfO_2[44,45]) polymers,[46] or halide electrolytes[47] as coatings. While recent advances have shown promising results in improving interfacial stability and enhancing battery performance, long-term stability, scalability, and cost-effectiveness remain major challenges for practical implementation.

As recently reported by our group, the formation of an artificial CEI is a promising approach to prevent interfacial degradation.[48] This approach mimics the natural CEI formation of sulfide SEs during a controlled treatment, aiming to accommodate the driving force of the chemical reaction between sulfide SE and Ni-rich CAM while preventing harmful side reactions. So far, this concept has only been studied within a narrow parameter range, which is typical for most coating investigations reported in literature.

In general, various instrumental analytical techniques can be applied to characterize the coating morphology and composition.[49] However, not all of them are suitable for an efficient and systematic parameter study, due to difficulties in sample preparation or limited statistically relevant information that can be quantified. A possible approach is the combination of a high-throughput method, such as X-ray photoelectron spectroscopy (XPS), and further high-resolution techniques, such as scanning transmission electron microscopy (STEM), for a smaller number of selected samples. With respect to electrochemical performance, long-term cycling tests are usually carried out to prove a positive coating effect compared to a not-intentionally coated sample. However, this only allows for a proof-of-principle without further understanding of the coating mechanism and subsequent optimization of the coating parameters. Hereby, the true potential of the coating might be left undiscovered. Another drawback of long-term cycling experiments is that chemo-mechanical degradation of the full cell and anode-related contributions come into play.[50] They can easily interfere with the effects of cathode-electrolyte interface degradation and impede understanding of the actual effectiveness of the CAM coating in suppressing detrimental interfacial reactions. Chemo-mechanically improved battery cells, on the other hand, often require a slurry fabrication process, including wet processing with suitable solvents and binders, introducing more material combinations and interfaces, making it difficult to relate results directly to the SE|CAM interface.[44] In addition, a larger amount of CAM is needed during composite preparation, compared to lab-scale hand-grinding approaches. Especially during the development of new coating strategies, these larger quantities may not always be available. Thus, new experimental approaches are required to evaluate and benchmark the performance of coatings, such as recently proposed.[51]

One principal aim of this study is to demonstrate that such a systematic CAM coating investigation can be carried out in an efficient and effective way, which facilitates comprehensive understanding of the coating and enables further optimization. Therefore, in this work, we delve into the artificial CEI coating approach, and systematically examine the impact of annealing on CEI formation. We use Li_3PS_4 as sulfide SE and $LiNi_{0.85}Co_{0.10}Mn_{0.05}O_2$ (NCM85) as Ni-rich CAM. The second focus of this work is to gain a better understanding of the coating formation process. To achieve this, the SE was deposited on the CAM surface by a dry-coating approach. The SE-coated CAM was then annealed in synthetic air at various temperatures up to 700 °C. In the following, we employ a combined approach using analytical and electrochemical methods to gain insights into the effect of annealing on the coating properties. We show that the coating morphology as well as composition can be modified by tailored annealing, which has a significant impact on performance. We demonstrate the importance of investigating various process parameters during coating preparation to avoid too general and potentially misleading statements about the coating. Optimal properties of the proposed CEI coating and cell performance are achieved at moderate annealing temperatures, highlighting the versatility of this coating approach and providing guidance for further optimization.

EXPERIMENTAL SECTION

Cathode Active Material Coating. The cathode active material ($LiNi_{0.85}Co_{0.10}Mn_{0.05}O_2$, NCM85) was provided by BASF SE and dried under vacuum at 200 °C for 12 h prior to utilization. The coating was applied through dry-coating with mortar and pestle, followed by a heat treatment under synthetic air, similar to previous work by Zuo et al.[48] Accordingly, Li_3PS_4 (NEI Corporation) was added to NCM85 in a weight ratio of 1:99, and the mixture was hand ground for 30 min using an agate mortar. The mixed powder, i.e., SE-coated NCM, was pressed into pellets by a hand press

https://doi.org/10.1021/acs.chemmater.4c03086
Chem. Mater. 2025, 37, 2192−2203

and transferred in a snap cap vial into a tube furnace. The annealing was done in synthetic air (118.5 sccm N_2 and 31.5 sccm O_2 flow). The temperature was increased with a heating rate of 2 K/min, and the final annealing temperature (up to 700 °C) was held for 1 h. After cooling down to room temperature and transferring the sample back to the glovebox, the pellet was hand ground for 5 min to get loose coated CAM powder, which was investigated further. Besides the transfer to and from the oven in a snap cap vial, all samples were treated in an argon-filled glovebox ($p(O_2)/p$ < 0.1 ppm, $p(H_2O)/p$ < 1.0 ppm).

Thermogravimetric Analysis−Mass Spectrometry (TGA-MS). Measurements were performed on a NETZSCH STA-409-PC coupled with a mass spectrometer QMS 403 Aëolos under synthetic air. About 20 mg of the Li_3PS_4 powder was placed in an alumina crucible and heated up to 800 °C.

X-ray Photoelectron Spectroscopy (XPS). XPS analyses were performed using a PHI5000 Versa Probe II system (Physical Electronics Inc.). The powders were filled into Teflon crucibles (inner diameter: 3 mm) and attached to the sample holder using nonconductive adhesive tape. All samples were transferred under argon using a transfer vessel for PTS sample holders by PREVAC. Monochromatic Al−K_α radiation (1486.6 eV) was applied for XPS analysis. The X-ray source was operated at a power of 50 W and a voltage of 17 kV. The analysis spot diameter was set to 200 μm. For charge compensation, a dual beam charge neutralization (ion beam combined with a low-energy electron beam) was used during measurements. The pass energy of the analyzer was 29.35 eV. The XPS data were evaluated using CasaXPS (Casa Software Ltd.). The spectra were calibrated in relation to the signal of adventitious carbon at 284.8 eV. For signal fitting, GL[30] line shapes and Shirley background were applied. Common fitting restrictions (e.g., theoretical signal area ratios depending on the analyzed orbital, fwhm constraints, and published values for spin orbit splitting) were used.

Scanning Transmission Electron Microscopy (STEM). The sample preparation was performed in an argon-filled glovebox with oxygen residues of $p(O_2)/p$ < 1.0 ppm and water residues of $p(H_2O)/p$ < 1.0 ppm. Here, the bare and coated particles were spread onto on carbon film-coated Cu-mesh TEM grids. These grids were then loaded into an inert/vacuum transfer holder (from Mel-Build) and transferred to the TEM under argon atmosphere to avoid reaction of the samples with air. A double Cs-corrected JEOL-JEM2200FS STEM, operating at 200 kV, was used for STEM imaging in the low annular dark-field regime. EDX maps were recorded using a Bruker Nano XFlash Detector 5060.

Low Energy Ion Scattering (LEIS). LEIS measurements were performed at IONTOF GmbH using a Qtac100 low-energy ion scattering spectrometer. Due to its high surface sensitivity, LEIS typically requires in-vacuum cleaning of samples prior to analysis to remove adsorbed species, as the standard method of atomic oxygen cleaning was not applicable for these samples. Spectra were recorded at room temperature, 100 °C, 200 °C, 400 °C, and 600 °C. The instrument is equipped with a double-toroidal analyzer with a fixed scattering angle of 145°. This setup maximizes the measurement sensitivity to keep the ion-beam induced sample damage within the static regime while still obtaining spectra with low noise levels. All samples were analyzed using a 3 keV $^4He^+$ ion beam at normal incidence, with an ion beam current of 2.6 nA scanned over an analysis area of 2 × 2 mm^2. With an acquisition time of 120 s per spectrum, this results in an ion fluence of $5 \cdot 10^{13}$ ions/cm^2, well within the static limit for a 3 keV $^4He^+$ analysis ion beam.

Cell Fabrication and Cycling. For the fabrication of solid-state battery cells, commercially available Li_6PS_5Cl (NEI Corporation) was used without further modification. The Li_6PS_5Cl SE was received and stored in an argon-filled glovebox to maintain its integrity, with oxygen residues of $p(O_2)/p$ < 1.0 ppm and water residues of $p(H_2O)/p$ < 1.0 ppm. The composite cathodes were composed of (un)coated NCM and Li_6PS_5Cl with a mass ratio of 80:20 wt %. No carbon additives or binders were used. The mixture was hand ground in an agate mortar for 15 min.

The basic cell setup used in this study is described in a previous publication.[52] As separator, 60 mg of Li_6PS_5Cl was pressed by hand. About 12 mg cathode composite was added on one side of the separator and distributed evenly. This side of the cell was closed with a modified steel stamp with an Al_2O_3 inlet as current collector to enable advanced post-mortem analysis of the composite cathode as reported by Hertle et al.[51] Afterward, the stacked pellet was pressed at 375 MPa for 3 min. On the other side of the separator, an indium foil (Alfa Aesar, 99.99%, 9 mm diameter, 100 μm thickness) and a lithium foil (China Energy Lithium, 6 mm diameter, 100 μm thickness) were placed to form the In/InLi anode. The complete cell was held in an aluminum frame at a constant pressure of 50 MPa (10 N m torque) during the electrochemical measurements. The cells were cycled at 0.05C (calculated based on a specific capacity of 200 mAh/g) between 1.9 and 3.7 V vs. In/InLi for 1.5 cycles (charge−discharge−charge) and relaxed overnight until the start of the ToF-SIMS measurement.

Time-of-Flight Secondary Ion Mass Spectrometry (ToF-SIMS). ToF-SIMS measurements were performed on a TOF-SIMS 5−100 by IonTOF GmbH Germany, which is equipped with a 25 keV Bi cluster primary ion gun for SIMS analysis. The full cell samples were prepared in an argon-filled glovebox. Insulating adhesive tape was used to attach the composite cathodes to the sample holder. The samples were transferred to the instrument under inert atmosphere using the transfer system Leica EM VCT500 (Leica Microsystems). The analysis area was 150 × 150 μm^2 and rasterized with 256 × 256 pixels (random mode). All measurements were performed in negative ion mode with 25 keV Bi_3^+ primary ions with a dose of $1 \cdot 10^{12}$ ions/cm^2 and a cycle time of 60 μs in spectrometry mode. The data were calibrated with the software SurfaceLab 7.3 (IONTOF GmbH). Pixel-by-pixel normalization (see[51] for details) was used for data analysis in this study. The analysis was performed through an in-house Python code,[53] which performed the pixel-by-pixel analysis on all the peaks identified as relevant. The data are scaled by the total ion count. For each sample, at least 14 different regions were analyzed to obtain statistically relevant information.

Tape-Cast Electrode Preparation. Uncoated and coated NCM85 (annealed at 400 °C) was used for slurry-cast electrode preparation following previous work.[45] Anhydrous o-xylene (97%, Sigma-Aldrich) as solvent, Super C65 carbon additive (TIMCAL Ltd.), and polyisobutylene binder (Oppanol N 150, BASF SE) were used in the preparation of the slurry. A composite cathode was first prepared by ball-milling (FRITSCH GmbH) CAM, SE, and Super C65 in a weight ratio of 69.3:29.7:1.0 at 140 rpm for 30 min. The as-prepared cathode composite was further wetted by o-xylene

https://doi.org/10.1021/acs.chemmater.4c03086
Chem. Mater. 2025, 37, 2192−2203

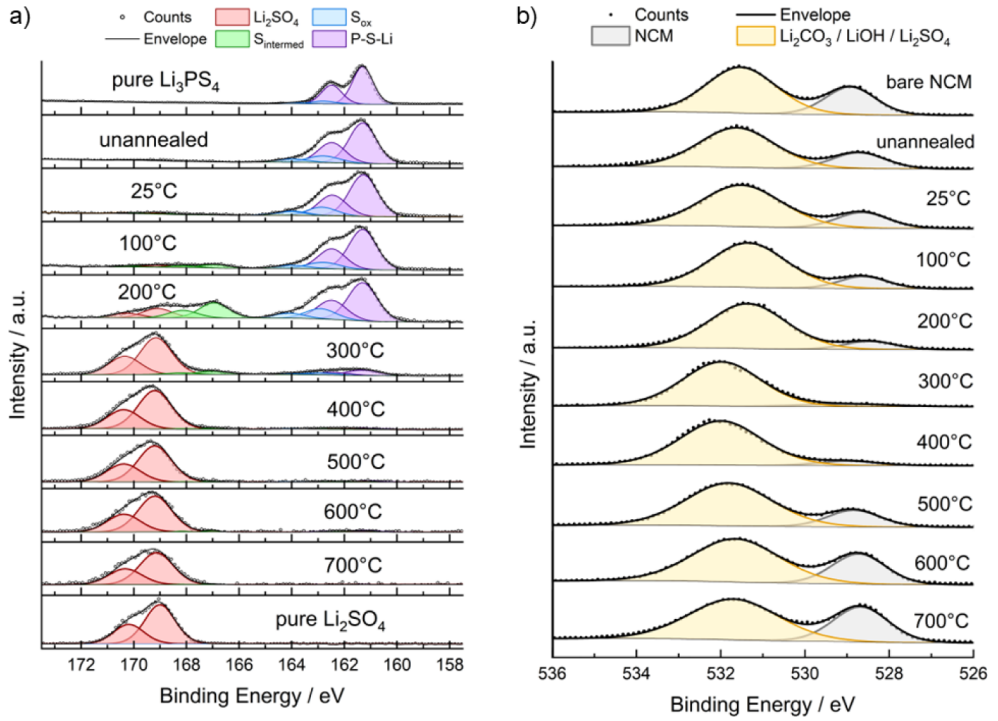

Figure 1. (a) XP detail spectra of the S 2p signal indicating the coating composition depending on the annealing temperature. With increasing temperature, the precursor Li_3PS_4 (E_B = 161.2 eV) transforms into Li_2SO_4-like species (E_B = 169.4 eV). (b) XP detail spectra of the O 1s signal monitoring the evolution of the NCM lattice oxygen signal (gray) and the oxygen signal stemming from surface impurities/coating (yellow). Lower NCM signals suggest increased coating coverage.

with a fixed solid content of 64 wt % and mixed at 600 rpm for 2 min in a centrifugal planetary mixer. The binder solution was then added dropwise to the wetted composite in a weight ratio of 1:99 (binder:cathode composite), followed by further mixing at 2000 rpm for 6 min. Next, the slurry was cast onto Al foil using a mini tape casting device from MTI Corp. All preparation steps were conducted under inert atmosphere either in a sealed container or inside an argon-filled glovebox. The as-prepared cathode sheet was first dried in the glovebox at room temperature for 4 h, then under vacuum for another 12 h. Finally, the cathode tape was punched into discs with a diameter of 9 mm for further electrochemical testing. The assembling procedure was the same as that for the pelletized cells described above, and the cells were cycled between 2.28 and 3.68 V vs. In/InLi.

RESULTS AND DISCUSSION

The sulfide solid electrolyte Li_3PS_4 (LPS) was dry-coated onto polycrystalline NCM85 and then annealed at temperatures between 25 and 700 °C under synthetic air for 1 h to form a coating mimicking the natural CEI. For each artificial CEI coating, both the morphology and the chemical composition were investigated first. In this work, we focused on X-ray photoelectron spectroscopy (XPS) combined with additional scanning transmission electron microscopy (STEM), energy-dispersive X-ray spectroscopy (EDX), and low-energy ion scattering (LEIS) measurements on selected samples. Afterward, all coatings were tested electrochemically in pelletized cells, and the degradation products were analyzed *post mortem* via time-of-flight secondary ion mass spectrometry (ToF-SIMS).

Characterization of Coating Composition and Coverage via XPS and LEIS. XPS analysis as a surface-sensitive technique was performed to monitor compositional changes in the coating, as well as changes in the coating coverage due to the variation in temperature. The aim of the temperature treatment is to oxidize the LPS coating precursor, involving synthetic air as an alternative oxygen source to prevent damage to the CAM. Oxygenated sulfurous- and phosphorous species are formed in these reactions, whereby both (partially lithiated) Li_xSO_y, Li_xPO_y, and mixed phases, such as $Li_xS_yP_zO_v$, are conceivable. Thus, changes in composition were tracked with the S 2p (Figure 1a) and P 2p detail spectra (Figure S1).

The S 2p peak at a binding energy around 161.2 eV corresponds to sulfur in the form of PS_4^{3-} in the LPS precursor, while the S 2p peak around 169.4 eV indicates the formation of sulfates.[33] As seen in Figure 1a, after annealing at 25 °C in synthetic air, the coating precursor has not significantly reacted. The main contributions in the S 2p spectrum match well with the pristine LPS measured as reference. The same accounts for the P 2p spectrum. With increasing annealing temperature, successive transformation of the coating precursor is observed in the S 2p and P 2p spectra. The precursor starts to oxidize to a greater extent between 100 and 200 °C, and the conversion seems to be completed at around 400 °C. The corresponding energy positions indicate the formation of Li_2SO_4- and Li_3PO_4-like species, and thus the intended transformation. With a further rise in temperature above 400 °C, no further changes in the signal shape are observed in the S 2p and P 2p spectra. However, the overall intensity of both decreases, already indicating a removal of coating material.

The compositional evolution is additionally supported by changes in the O 1s signal region (Figure 1b). For the bare NCM, two principal peaks in the O 1s spectrum can be differentiated, which are attributed to the lattice oxygen of the

https://doi.org/10.1021/acs.chemmater.4c03086
Chem. Mater. 2025, 37, 2192−2203

NCM at lower binding energy ($E_B \approx 528.7$ eV) and to Li_2CO_3/LiOH impurities at higher binding energy (~531.4 eV), both of which are typically found on the surface of NCM particles.[54,55] The latter peak can also be seen for the coated samples, but they overlap with contributions originating from Li_2SO_4- and Li_3PO_4-like species, which can be found at slightly higher binding energies of about 532 and 532.5 eV, respectively.[56,57] Accordingly, the signal position of the combined peak shifts to higher binding energies for moderate annealing temperatures (300 and 400 °C), due to the formation of Li_2SO_4- and Li_3PO_4-like species, and shifts back toward the original position for temperatures above 500 °C, also indicating evaporation/sublimation of the coating.

The effect of coating removal can be more clearly seen in the NCM lattice oxygen contribution at around 528.7 eV depending on annealing temperature (Figure 1b). For the unannealed sample, the contribution is reduced compared to the bare NCM, indicating that the precursor covers the NCM surface. With increasing temperature, the intensity of the NCM lattice oxygen contribution is successively decreasing to a minimum for the sample annealed at 300 °C. At this temperature, no NCM lattice oxygen can be detected indicating that the particles are covered with a layer of at least 10 nm. This thickness corresponds approximately to the depth of information in XPS measurements. A further increase of annealing temperature leads again to a rise in lattice oxygen contribution, which indicates that the NCM surface is successively exposed and the coverage decreases. After annealing at 700 °C, the contribution is even higher than for the uncoated reference sample, suggesting that in addition to the removal of coating material, also the common surface impurities (e.g., Li_2CO_3 and LiOH) are partially removed.

A similar trend concerning the coating coverage can be derived from the Ni 2p signal (Figure S2). The decrease in the Ni 2p signal up to an annealing temperature of 300 °C indicates that the transformation of the coating precursor is accompanied by an increasing coverage of the NCM, since XPS is a surface sensitive technique and the NCM:LPS mass ratio was the same in all cases. By comparing the signal intensities of the Ni 2p (CAM) and S 2p/P 2p (coating) detail spectra, the coverage was semiquantitatively evaluated. For this purpose, we used the sum of the relative intensities of the S 2p and P 2p signals for the coating, $I_{coating}$, and the Ni 2p signal for the CAM, I_{CAM}. According to eq 1, the degree of coverage, γ, can reach values between 0 ("not" covered) and 1 ("fully" covered):

$$\gamma = \frac{I_{coating}}{I_{coating} + I_{CAM}} \quad (1)$$

The values for the differently annealed samples are depicted in Figure 2. A maximum coverage for annealing at 300 °C and a decreasing coverage at higher annealing temperatures are found, which confirms the previously discussed observations. It should be noted that the coverage values only serve as an indicator to allow for a comparison among the samples. The calculated values cannot be considered as the real coverage, since the signal intensities are also affected by the coating layer thickness and surface impurities contribute to a lower NCM signal, although they are not part of the intentional coating. Due to the spatial resolution of XPS no single particles are measured but instead statistical information is obtained by analyzing more than 1500 particles simultaneously. Apart from

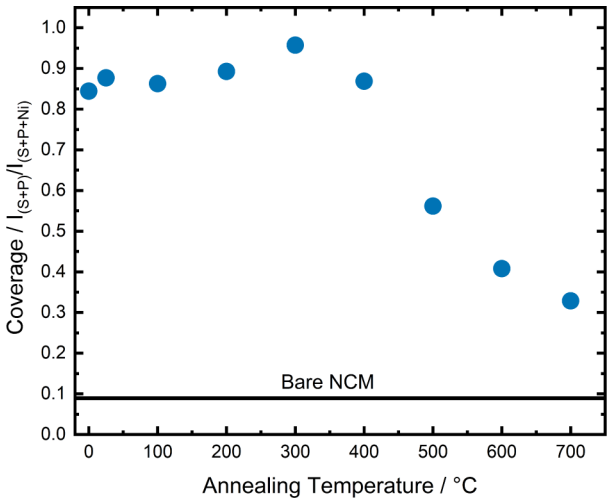

Figure 2. Coating coverage as a function of annealing temperature (hereby 0 °C means unannealed), approximated from relative XPS intensities. Signal intensities (at. %) of coating elements (S, P) are evaluated with respect to the Ni signal stemming from the NCM.

eq 1, other methods of expressing the degree of coverage are feasible. For instance, one could consider the relative Ni signal without any further calculations (Figure S3). All approaches lead to the same trend, allowing for a semiquantitative comparison of the coating coverage by XPS indicating that the annealing temperature affects the coverage and thickness of the coating layer.

The XPS results are supported by thermogravimetric analysis (TGA) combined with mass spectrometry (MS) measurements, carried out under synthetic air on the pure precursor material LPS (Figure S4). After an initial slight weight loss, e.g., due to previous hydrolysis, LPS is stable up to ~180 °C. At an onset temperature of 180 °C, oxidation with mass increase occurs. This ends at about 300 °C, which is consistent with the conclusions on the coating coverage drawn from the XPS analysis. At ~320 °C, oxidation/decomposition begins with a primarily endothermic loss of mass, which is completed at around 380 °C. Especially the second part of the reaction is accompanied by the evolution of SO ($m/z = 48$) and SO_2 ($m/z = 64$). We note that also signals with $m/z = 50$ and $m/z = 66$ can be detected between 300 and 400 °C, corresponding to POH_3 and PO_2H_3, respectively. However, their intensity is lower, by 1 order of magnitude, than that for the sulfurous species. From 400 °C onward, successive slight weight loss is detected. Accordingly, the main reactions occur between 200 and 400 °C, and the trend in coating coverage derived from XPS correlates well with the TGA data. At higher temperatures, the coating precursor starts to evaporate, which is accompanied by SO, SO_2, POH_3, and PO_2OH_3 evolution. Based on these results, TGA analysis of the SE coating precursor should be considered as a useful precharacterization method for narrowing the range of annealing temperature for coating preparation optimization.

Low energy ion scattering (LEIS) was further carried out to gain more surface sensitive information. Figure 3 depicts the LEIS spectra of three coated NCM samples annealed at different temperatures, along with a bare reference sample, all heated to 200 and 600 °C inside the LEIS device before analysis to remove surface adsorbates. The labeled surface peaks represent the elemental composition of the outer atomic

https://doi.org/10.1021/acs.chemmater.4c03086
Chem. Mater. 2025, 37, 2192−2203

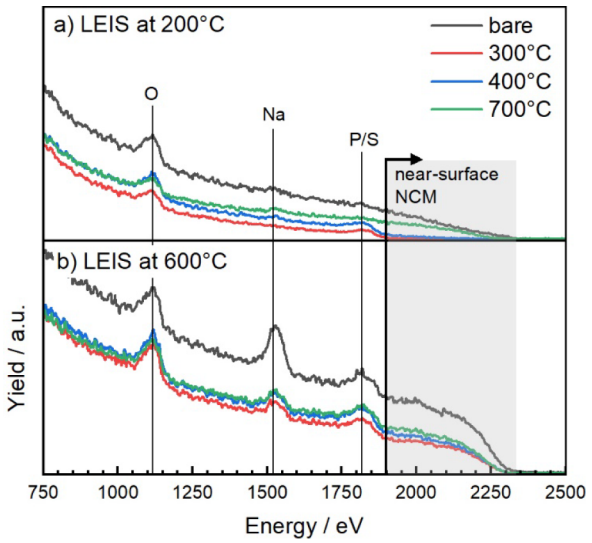

Figure 3. LEIS spectra (taken with 3 keV $^4He^+$) of bare and coated NCM annealed at 300, 400, and 700 °C after heating to (a) 200 °C and (b) 600 °C in the LEIS device.

layer. The absence of a surface peak for Mn/Ni/Co, which were not resolved under these measurement conditions, indicates that no metal atoms from the base material are present in the outer surface layer. However, most of the baseline of the spectrum is due to subsurface NCM atoms, with lower energy values corresponding to greater depth. All signal intensity at energies of 1900 eV and higher originates from NCM atoms in near-surface layers at a depth of 1 to 3 nm. At 200 °C measurement temperature (Figure 3a), these near-surface NCM signals are significantly reduced for the coated samples annealed at 300 and 400 °C, indicating the presence of a coating. Also, for the coated sample annealed at 700 °C a small signal reduction compared to the bare NCM is observed. With increasing temperature in the measurement device, the situation changes. At 600 °C (Figure 3b), the subsurface NCM signal strongly increases for samples annealed at 300 and 400 °C compared to the spectrum shown in Figure 3a. This suggests an increased fraction of NCM just below the surface, meaning that the coating thickness and coverage are decreased. The coated sample annealed at 700 °C shows this behavior from the beginning, presumably because it was already annealed to such a high temperature during the coating process. The reason for the overall higher intensity of the spectra recorded at 600 °C is probably related to some change in surface chemistry, which increases the reionization of He. However, further investigations are required to elucidate this aspect. The occurring sulfur/phosphorus peak for the bare NCM at 600 °C might stem from impurities of the coprecipitation step during the NCM synthesis. Such sulfur residuals were already observed in a previous work by EDX and ToF-SIMS.[58] Sodium is a typical surface contamination, which is often detected in LEIS measurements.[59] Overall, when measuring at 600 °C, the spectra look qualitatively almost identical for all samples, which is probably due to the removal of coating at elevated temperatures. Accordingly, the coated samples become similar to the uncoated NCM, which overall is in agreement with the previously described XPS and TGA-MS results.

Characterization of Coating Morphology via STEM-EDX. LAADF STEM investigations were conducted on selected samples to gain visual information on the coating morphology at the nanoscale (Figure 4). While no coating

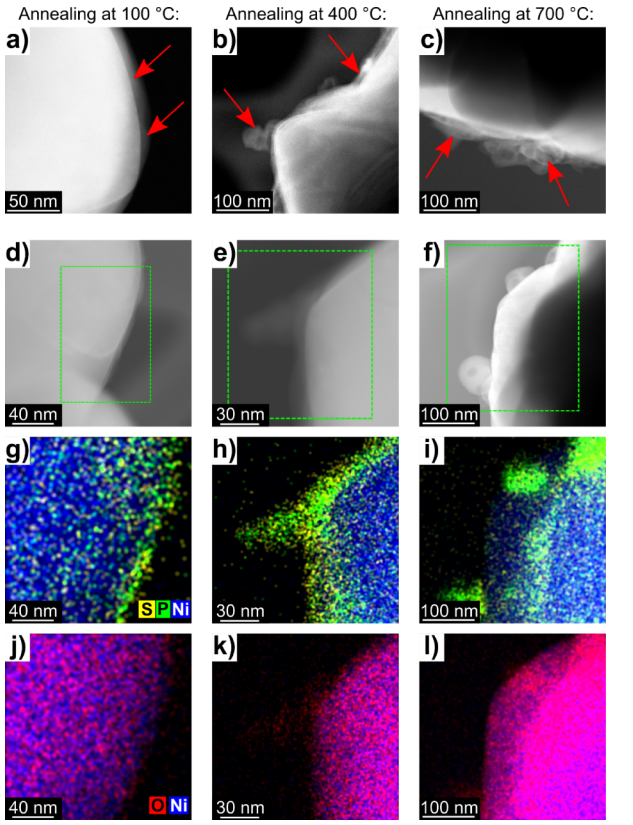

Figure 4. Low-angle annular dark field (LAADF) STEM and STEM-EDX images of LPS-coated NCM85 annealed at 100 °C (a, d, g, j), 400 °C (b, e, h, k), and 700 °C (c, f, i, l). Red arrows indicate the coating and green boxes the area probed using EDX.

layer is visible for the bare NCM (Figure S5), the LPS-coated particles show different coating morphologies depending on the annealing temperature. For the coated sample annealed at 100 °C, a relatively uniform layer of 5 to 20 nm thickness is found (Figure 4a,d), indicating successful dry-coating. However, occasionally we found larger coating particles (Figure S6), which confirms the assumption that the surface layer is not completely homogeneous after the simple coating approach based on hand grinding used in this work. In general, the coating preferably accumulates in notches between the primary particles (Figure S7). The morphology significantly changes with increasing annealing temperature. After annealing at 400 °C, a relatively thick (20 nm−50 nm) and rough coating is found (Figure 4b,e). Additionally, some coagulation is observed, which leads to the formation of medium to large coating particles. The highest annealing temperature of 700 °C results in the formation of even larger particles (50 nm−120 nm) with almost no coating in between (Figure 4c,f). Apparently, the coating underwent a morphological transformation by removal of thin layers and aggregation into larger particles.

STEM-EDX confirmed the previous results with respect to the coating composition. Sulfur and phosphorus were detected in all samples irrespective of the annealing temperature (Figure 4g−i). However, oxygen signals were only detected in the samples annealed at 400 and 700 °C (Figure 4k,l). No oxygen

https://doi.org/10.1021/acs.chemmater.4c03086
Chem. Mater. 2025, 37, 2192−2203

was observed in the coating of the sample annealed at 100 °C (Figure 4j), indicating the coating precursor was not yet oxidized, as expected from the XPS investigations. We like to note that the coating and particles are quite sensitive to the electron beam and degrade under the strong irradiation during EDX measurements. Changes in coating morphology during the EDX measurements are thus unavoidable.

Overall, the characterization results demonstrate that the coating properties are not fully determined during the mechanical dry-coating process, but can be tailored during annealing. Not only the composition, but also the morphology of coating can be adjusted by controlled annealing. With a tailored annealing program, it seems feasible to further optimize the coating with respect to coverage and thickness (see also Section S1).

Electrochemical Performance. To examine the influence of the coating composition and morphology on electrochemical performance and the interfacial processes within the composite cathode, systematic cell cycling with subsequent *post mortem* analysis using ToF-SIMS was performed in accordance with a benchmarking approach reported earlier.[51] The cells consisted of a Li_6PS_5Cl (LPSCl) separator, an In/InLi anode and a cathode composite of NCM and LPSCl. They underwent only 1.5 cycles (charge−discharge−charge) and a relaxing step overnight before the ToF-SIMS measurement, allowing for time-efficient benchmarking of the coating performance.

From the short-term cycling results, various metrics can be extracted and taken into consideration to assess the electrochemical performance of the coatings. First, the initial Coulomb efficiency (ICE) is a good indicator for the interfacial decomposition of SE. In SSBs, the significantly larger first-cycle charge capacity stems from the oxidative decomposition of SE.[31,60] It is therefore often the case that a higher ICE indicates lower initial SE decomposition. As depicted in Figure 5a, the ICE reaches around 85% for the uncoated sample. Interestingly, for the lower annealing temperatures up to 200 °C, the coated samples show even lower ICEs. For annealing temperatures of 300 °C and above, the ICE improves compared to the bare NCM. This already indicates that coating composition and morphology significantly affect interfacial reactions and thus the electrochemical properties and that a coating does not always lead to an improvement. The absolute capacities follow a similar trend, for which the 700 °C sample reaches the highest second-cycle specific charge capacity of 199.5 mAh/g. Here, apart from the 25 °C sample, all coatings lead to an improvement compared to the composite using bare NCM. However, from these results alone, no firm conclusions can be drawn about the quality of coating depending on the annealing temperature.

Since the measurable capacities strongly depend also on the microstructure of the cathode composite which in turn depends on the mixing process, additional parameters, such as overpotential, as measure for the internal resistance were considered. When galvanostatically charging the cell, the upper cutoff voltage, here 3.7 V vs. In/InLi, is reached while the actual state-of-charge (SOC) of the CAM is lower. Analogously, when discharging the cell, the lower cutoff voltage, here 1.9 V vs. In/InLi, is reached while the actual SOC of the CAM is higher. Thus, during a following OCV period in both cases, the potential relaxes toward the actual SOC of the system. A stronger relaxation is the consequence of a higher overpotential during charging/discharging and indicates a

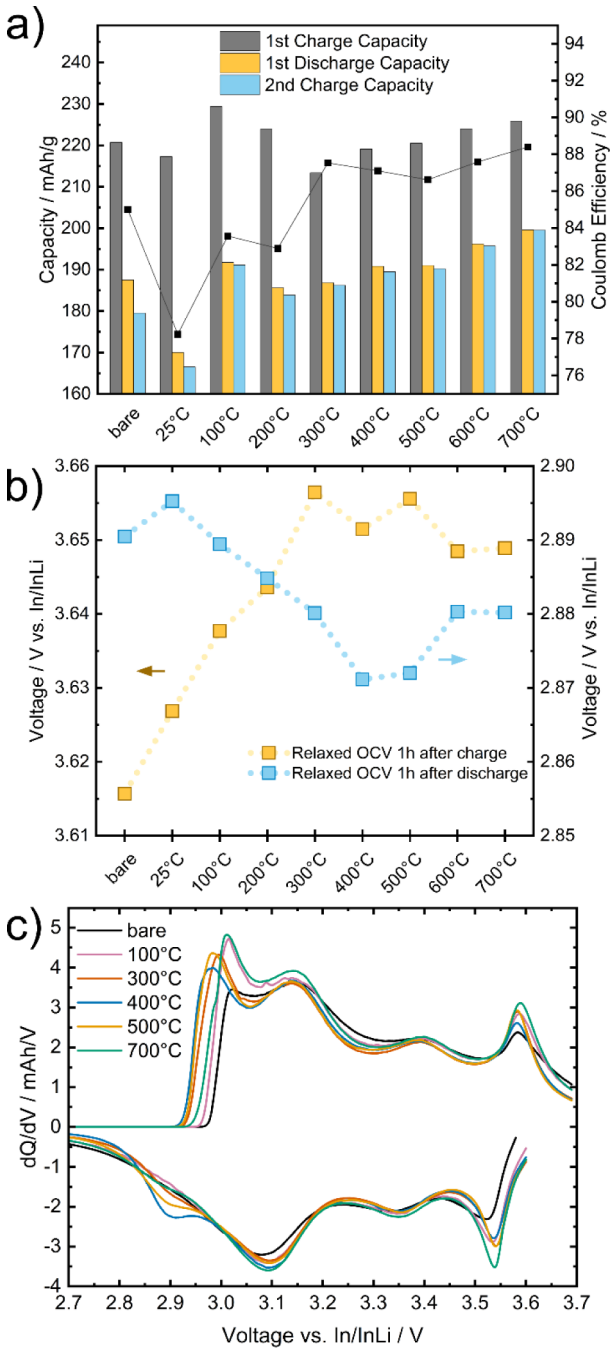

Figure 5. Electrochemical parameters used for comparison of the coating effects including (a) the specific capacities of 1.5 cycles, (b) the relaxed OCV reached after 1 h after galvanostatic charging/discharging to 3.7/1.9 V vs In/InLi, and (c) differential capacity plots of the first discharge and second charge cycles.

larger cell resistance. Since the tested cells were built identically, a difference in cell resistance should be mainly attributed to the CEI degradation layer. Comparing the relaxed potentials 1 h after charging/discharging, as depicted in Figure 5b, allows a ranking of the coating quality. The relaxed potentials are maximal after charge and minimal after discharge for the samples annealed at 300 to 500 °C. Lower annealing temperatures lead to a significantly larger potential relaxation, indicating higher cell resistance. Also, higher annealing temperatures lead to a slightly stronger relaxation. This trend is confirmed by the differential capacity plots of the first

https://doi.org/10.1021/acs.chemmater.4c03086
Chem. Mater. 2025, 37, 2192−2203

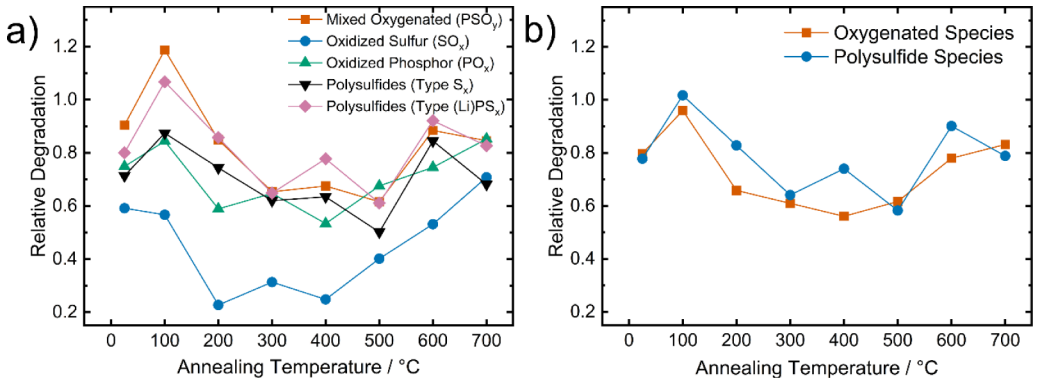

Figure 6. ToF-SIMS surface analysis to determine the relative degradation of composite cathodes with differently annealed LPS-coated NCMs. The signal intensity of each fragment is normalized to the respective total ion signal before calculating the relative degradation, which corresponds to the relative intensity of the signal with respect to the signal of a composite cathode using uncoated NCM.

discharge and second charge cycles (Figure 5c). In general, the overpotential is found to be decreased for all coated samples compared to the bare NCM. However, the samples annealed at medium to high temperatures clearly show a reduced overpotential compared to coated samples treated at lower or higher temperatures. During discharge, the samples annealed at 400 and 500 °C show an additional feature at ∼2.9 V vs In/InLi, which is commonly referred to as "kinetic hindrance" region and is considered as a beneficial feature.[61] Overall, the electrochemical results are in accordance with the XPS, TGA-MS, LEIS, and STEM/EDX results: Annealing between 300 and 500 °C leads to an optimized coating, which in turn improves the performance from an electrochemical perspective.

Post-Mortem ToF-SIMS Degradation Analysis. After the short-term cycling, ToF-SIMS measurements were carried out to detect and quantify degradation products. The combination of electrochemical data and *post mortem* analysis is imperative to holistically compare different coatings.[51] Considering the strong correlation between the EC performance and the interfacial degradation, the resulting side products during cycling will be discussed thoroughly in the following section. While the electrochemical performance (in terms of achievable capacity and capacity retention) should be as high as possible, the relative degradation product signals should be as low as possible.

In general, interfacial degradation between NCM and sulfide SEs can be divided into two pathways.[51] One is arising from the SE being in contact with electronically conducting surfaces, i.e., the current collector, CAM surface, or carbon additives, leading to electrochemical oxidation through lithium extraction, e.g., formation of polysulfide species.[31] They do not necessarily have to be regarded as detrimental, since the as-formed compounds can be assumed to be redox active within a certain potential range, but they may increase local resistance.[35,62,63] The other type of degradation is arising from the chemical, oxygen-involving oxidation of the SE being in contact with the CAM particles. Thereby, sulfites/sulfates (Li_xSO_y), phosphites/phosphates (Li_xPO_y), and thiophosphites/thiophosphates ($Li_xS_yP_zO_u$) are generated as parasitic byproducts, as well as gaseous reaction products. Since the oxygen originates from the NCM, the reactions are accompanied by surface reconstruction with rock-salt phase formation, which is known to impede lithium transport.[30,36] Our coating approach intends to minimize the damage to the CAM and the associated more or less "uncontrolled" reactions with the SE.

To investigate the effect of the coatings on interfacial reactions, ToF-SIMS measurements were performed. In the analysis, the ion fragments can be assigned to different groups of degradation products, as depicted in Figure 6a. Herein, the results of principle component analysis (PCA) were used to weight the intensity of the corresponding fragments appropriately (cf. ref 51 for details). The signals were normalized with respect to the uncoated sample to directly see the influence of the coating on the ion fragment intensities. Relative degradation values above 1 indicate that more degradation products were detected for the sample than for the bare reference material, while values below 1 indicate the opposite trend. For better visualization, we further grouped the fragments from Figure 6a into the two main (solid) degradation products (polysulfide-like and oxygenated species) in Figure 6b.

Compared to the bare reference sample, almost all coatings lead to a decrease in degradation products, even though the coating itself consists of oxygenated sulfurous and phosphorous species. However, there are distinct differences for the different annealing temperatures, and a clear trend is apparent. Apart from the sample annealed at 100 °C, the degradation products successively decrease with increasing annealing temperature down to a minimum for the coatings annealed between 300 and 500 °C. At higher annealing temperatures, the trend in coating coverage and electrochemical data is reflected by the increased fraction of degradation products. Higher annealing temperatures lead to partial removal of the coating, resulting in more reactive CAM|SE interfaces, which in turn results in an increase in side products. Accordingly, the less the coverage, the higher the electrochemical performance in terms of initial capacity, but also the fraction of degradation products.

Overall, the coating seems suitable to mitigate interfacial reactions between NCM and SE, resulting in smaller fractions of both oxygenated sulfurous/phosphorous species and polysulfides. Particularly the latter is remarkable, since the coating itself already consists of oxygenated sulfurous/phosphorous species. According to the data shown so far, the best compromise between coating morphology/composition, electrochemical performance, and degradation products can be found for the coated CAMs annealed at 300 and 400 °C. Although the bare NCM surface initially provides a higher

https://doi.org/10.1021/acs.chemmater.4c03086
Chem. Mater. 2025, 37, 2192−2203

capacity in the initial charge cycle, it suffers from significant interfacial degradation and overpotential, which is expected to result in inferior long-term cycling performance compared to the coated samples.

Long-Term Cycling Performance. To verify the predicted improved long-term performance, cells with slurry-cast cathode sheets were cycled over a longer period of time. The aim is to reduce the influence of chemo-mechanical degradation, which is a severe problem in pelletized cells that have been used for short-term cycling.[50] A disadvantage of slurry-cast electrodes is that relatively larger amounts of coated material are required, which are often not easily available for small batch testing in lab scale. Thus, in our case, only the coated sample annealed at 400 °C was chosen for long-term cycling experiments, since it provides a fully oxidized coating, which is not the case for the sample annealed at 300 °C. The corresponding electrochemical performance is shown in Figure 7. The coated sample reaches a significantly higher ICE

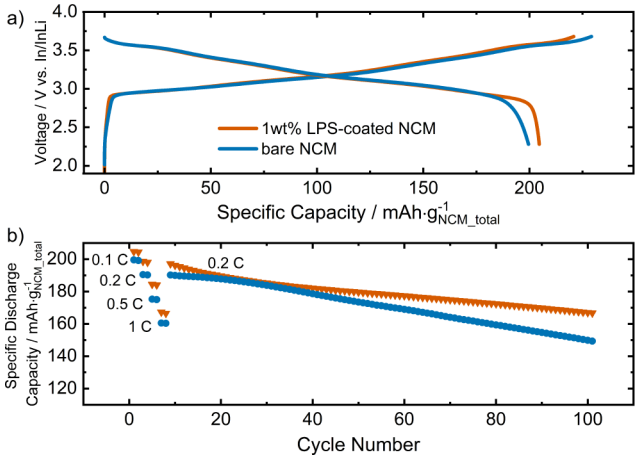

Figure 7. Cycling performance of the uncoated and LPS-coated NCM in a full cell with tape casted electrodes. (a) First-cycle voltage profiles at C/10 and (b) specific discharge capacities calculated with respect to the total mass of NCM in the composite cathode over 100 cycles (at C/5 after initial rate capability testing).

(92.7%) compared to the uncoated NCM (87.1%) and a first-cycle specific discharge capacity of almost 205 mAh/g. The capacities were calculated with respect to the total mass of NCM in the composite cathode. In the following, the C-rate was gradually increased from 0.1 to 1.0C. The SE-coated CAM delivered specific discharge capacities of 204, 198, 184, and 166 mAh/g at 0.1, 0.2, 0.5, and 1.0C, respectively, i.e., about 97, 90, and 81% of the capacity achieved at 0.1C was retained at higher C-rates. In contrast, the specific discharge capacities and their retention were lower for the bare NCM85 (199/190/175/160 mAh/g at 0.1/0.2/0.5/1.0C). Also, during long-term cycling at 0.2C, the coated sample proves its improved long-term performance, retaining 85% (vs 79% for the uncoated counterpart) of the capacity after 90 cycles. It should be noted that practically also the anode can significantly contribute to capacity fading during long-term cycling and its influence is not well controlled in a two-electrode cell configuration. However, based on the statistics, at least two independent cells were measured and presented the same trend, thus corroborating the significantly enhanced performance by the introduced coating and reducing the interference from the anode. During cycling, the SE oxidation and CEI growth continue, leading to a continuously increasing interfacial resistance, which in turn lowers the capacity during galvanostatic cycling. These processes are effectively mitigated by the SE-coated sample, thus leading to improved long-term performance.

Discussion of the Artificial CEI Coating. Cathode active material coatings are frequently not subjected to systematic analysis and optimization in the literature. Consequently, the influence of different process parameters on the microstructure, composition, and performance may remain undiscussed, and the true potential of coatings cannot be accurately assessed. At the same time, results are often referred to the coating material in general, although its properties may vary significantly depending on the process parameters. Rather than making generalized statements about the performance of a particular coating material, it is more prudent to consider the specific process parameters and their impact on the coating's microstructure, composition, and ultimately its performance.

As demonstrated in this work, not every coating leads to an improvement since the annealing temperature, for instance, has a crucial effect by influencing not only the composition, but also the morphology (coverage) of the coating. The highest coverage was obtained for an annealing temperature of 300 °C, while a fully oxidized surface layer required temperatures beyond 300 °C. To achieve both high coating coverage and full SE oxidation, we further investigated the influence of annealing time and gas atmosphere. Details of this investigation are presented in Section S1. It was found that a longer annealing time has a beneficial effect only if the oxidation is not completed after 1 h, that is, for temperatures below 400 °C. Increasing the oxygen partial pressure in the annealing atmosphere can accelerate the precursor oxidation at lower temperatures, allowing for shorter annealing times. The annealing not only affects the coating properties but may also alter the defect chemistry and structure of the cathode material.[24,64] To deconvolute these contributions and to fully elucidate the working principle of the artificial CEI coating, further systematic investigations are required in the future.

While already the annealing process allows for a significant optimization of the artificial CEI by adjusting the annealing temperature, time, and atmosphere, numerous other parameters may further improve the coating properties. The deposition method, with associated parameters, such as precursor amount, may enable a more uniform and thinner coating. Moreover, the precursor type can be varied, since all sulfide SEs are in principle applicable for that purpose, which may require again a reassessment of process parameters. Further optimization of all these parameters has the potential to enhance the performance of the artificial CEI coating approach. Thereby, a systematic benchmarking framework is able to facilitate and accelerate the optimization process. In general, the development and optimization of active material coatings remain an important and challenging task on the path toward stable solid-state batteries.

CONCLUSIONS

We have investigated the effect of annealing process on the properties of a CAM coating, which involves creating an artificial CEI prior to cell assembly. After applying the sulfide SE, Li_3PS_4, as coating precursor during a simple dry-coating process on polycrystalline $LiNi_{0.85}Co_{0.10}Mn_{0.05}O_2$, the annealing temperature was systematically varied. The resulting coatings were characterized in detail using XPS, TGA-MS, LEIS and STEM with respect to their morphology and

https://doi.org/10.1021/acs.chemmater.4c03086
Chem. Mater. 2025, 37, 2192−2203

chemical composition. The analyses revealed that both properties are strongly dependent on the annealing temperature. The temperature should be as high as necessary to ensure complete oxidation of the coating precursor and at the same time as low as possible to avoid evaporation or coagulation of coating. Further electrochemical testing and *post mortem* ToF-SIMS analysis showed that only a properly annealed coating leads to the intended mitigation of interfacial degradation. The corresponding temperature range was found to lie between 300 and 400 °C. Preliminary additional tests with respect to annealing time and gas atmosphere indicated that these process parameters can also significantly affect the coating quality. These results emphasize the versatility of the proposed coating approach.

Overall, our work highlights the importance of investigating different process parameters to fully explore the coating potential and to avoid too generalized statements. We have demonstrated that this can be achieved through efficient benchmarking, combining electrochemical tests as well as microscopic and spectroscopic/spectrometric methods.

■ ASSOCIATED CONTENT

Supporting Information

The Supporting Information is available free of charge at https://pubs.acs.org/doi/10.1021/acs.chemmater.4c03086.

XP spectra of the P 2p and Ni 2p signals for the un(coated) NCM, extracted relative Ni fraction as a function of temperature, TGA-MS for Li_3PS_4, additional STEM images of un(coated) NCM, and discussion of the effect of annealing time and atmosphere (PDF)

■ AUTHOR INFORMATION

Corresponding Author

Jürgen Janek − *Institute of Physical Chemistry, Justus Liebig University Giessen, Giessen 35392, Germany; Center for Materials Research (ZfM/LaMa), Justus Liebig University Giessen, Giessen 35392, Germany; Battery and Electrochemistry Laboratory (BELLA), Institute of Nanotechnology, Karlsruhe Institute of Technology (KIT), Karlsruhe 76131, Germany;* orcid.org/0000-0002-9221-4756; Email: juergen.janek@pc.jlug.de

Authors

Maximilian Kissel − *Institute of Physical Chemistry, Justus Liebig University Giessen, Giessen 35392, Germany; Center for Materials Research (ZfM/LaMa), Justus Liebig University Giessen, Giessen 35392, Germany;* orcid.org/0000-0001-9201-0748

Felix Walther − *Institute of Physical Chemistry, Justus Liebig University Giessen, Giessen 35392, Germany; Center for Materials Research (ZfM/LaMa), Justus Liebig University Giessen, Giessen 35392, Germany;* orcid.org/0000-0002-5843-4237

Jonas Hertle − *Institute of Physical Chemistry, Justus Liebig University Giessen, Giessen 35392, Germany; Center for Materials Research (ZfM/LaMa), Justus Liebig University Giessen, Giessen 35392, Germany;* orcid.org/0000-0001-8040-8038

Thomas Demuth − *Materials Science Center (WZMW) and Department of Physics, Philipps-University Marburg, Marburg 35032, Germany;* orcid.org/0009-0002-9796-4959

Ruizhuo Zhang − *Battery and Electrochemistry Laboratory (BELLA), Institute of Nanotechnology, Karlsruhe Institute of Technology (KIT), Karlsruhe 76131, Germany;* orcid.org/0000-0003-0292-5026

Philipp Brüner − *IONTOF GmbH, Münster 48149, Germany*

Torsten Brezesinski − *Battery and Electrochemistry Laboratory (BELLA), Institute of Nanotechnology, Karlsruhe Institute of Technology (KIT), Karlsruhe 76131, Germany;* orcid.org/0000-0002-4336-263X

Kerstin Volz − *Materials Science Center (WZMW) and Department of Physics, Philipps-University Marburg, Marburg 35032, Germany;* orcid.org/0000-0002-4456-5439

Complete contact information is available at: https://pubs.acs.org/10.1021/acs.chemmater.4c03086

Author Contributions

M.K.: conceptualization, formal analysis, investigation, visualization, project administration, writing original draft. F.W.: conceptualization, XPS and SIMS investigation, formal analysis, review and editing. J.H.: conceptualization, review and editing. T.D.: STEM-EDX investigation, review and editing. R.Z.: tape cast electrode investigation, review and editing. P.B.: LEIS investigation, review and editing. T.B.: supervision, review and editing. K.V.: supervision, review and editing. J.J.: conceptualization, supervision, funding acquisition, review and editing.

Notes

The authors declare no competing financial interest.

■ ACKNOWLEDGMENTS

This research was funded by the Deutsche Forschungsgemeinschaft (DFG, German Research Foundation)—within the priority program 2289 (heteroaggregates) under project no. 462470125 and by BASF SE. The authors acknowledge Dr. Alexander Sedykh for performing the TGA-MS measurement. Language and grammar of the manuscript have partially been improved with the help of *DeepL Write*.

■ REFERENCES

(1) Janek, J.; Zeier, W. G. A solid future for battery development. *Nat. Energy* **2016**, *1* (9), 16141.

(2) Sun, Y.-K. Promising All-Solid-State Batteries for Future Electric Vehicles. *ACS Energy Lett.* **2020**, *5* (10), 3221−3223.

(3) Alex, M. B.; Preger, Y.; Torres-Castro, L.; Katharine, L. H.; Stephen, J. H.; John, H. Are solid-state batteries safer than lithium-ion batteries? *Joule* **2022**, *6*, 742−755.

(4) Yu, X.; Chen, R.; Gan, L.; Li, H.; Chen, L. Battery Safety: From Lithium-Ion to Solid-State Batteries. *Engineering* **2023**, *21*, 9−14.

(5) Betz, J.; Bieker, G.; Meister, P.; Placke, T.; Winter, M.; Schmuch, R. Theoretical versus Practical Energy: A Plea for More Transparency in the Energy Calculation of Different Rechargeable Battery Systems. *Adv. Energy Mater.* **2019**, *9* (6), 1803170.

(6) Wang, R.; Cui, W.; Chu, F.; Wu, F. Lithium metal anodes: Present and future. *J. Energy Chem.* **2020**, *48*, 145−159.

(7) Jetybayeva, A.; Aaron, D. S.; Belharouak, I.; Mench, M. M. Critical review on recently developed lithium and non-lithium anode-based solid-state lithium-ion batteries. *J. Power Sources* **2023**, *566*, 232914.

(8) Huo, H.; Janek, J. Silicon as Emerging Anode in Solid-State Batteries. *ACS Energy Lett.* **2022**, *7* (11), 4005−4016.

(9) Franco Gonzalez, A.; Yang, N.-H.; Liu, R.-S. Silicon Anode Design for Lithium-Ion Batteries: Progress and Perspectives. *J. Phys. Chem. C* **2017**, *121* (50), 27775−27787.
(10) Han, Y.; Jung, S. H.; Kwak, H.; Jun, S.; Kwak, H. H.; Lee, J. H.; Hong, S.-T.; Jung, Y. S. Single- or Poly-Crystalline Ni-Rich Layered Cathode, Sulfide or Halide Solid Electrolyte: Which Will be the Winners for All-Solid-State Batteries? *Adv. Energy Mater.* **2021**, *11* (21), 2100126.
(11) Cronk, A.; Chen, Y.-T.; Deysher, G.; Ham, S.-Y.; Yang, H.; Ridley, P.; Sayahpour, B.; Nguyen, L. H. B.; Oh, J. A. S.; Jang, J.; Tan, D. H. S.; Meng, Y. S. Overcoming the Interfacial Challenges of LiFePO 4 in Inorganic All-Solid-State Batteries. *ACS Energy Lett.* **2023**, *8* (1), 827−835.
(12) Kim, T.; Kim, K.; Lee, S.; Song, G.; Jung, M. S.; Lee, K. T. Thermal Runaway Behavior of Li6PS5Cl Solid Electrolytes for LiNi0.8Co0.1Mn0.1O2 and LiFePO4 in All-Solid-State Batteries. *Chem. Mater.* **2022**, *34* (20), 9159−9171.
(13) Frankenberg, F.; Kissel, M.; Burmeister, C. F.; Lippke, M.; Janek, J.; Kwade, A. Investigating the production of all-solid-state battery composite cathodes by numerical simulation of the stressing conditions in a high-intensity mixer. *Powder Technol.* **2024**, *435*, 119403.
(14) Roitzheim, C.; Sohn, Y. J.; Kuo, L.-Y.; Häuschen, G.; Mann, M.; Sebold, D.; Finsterbusch, M.; Kaghazchi, P.; Guillon, O.; Fattakhova-Rohlfing, D. All-Solid-State Li Batteries with NCM−Garnet-Based Composite Cathodes: The Impact of NCM Composition on Material Compatibility. *ACS Appl. Energy Mater.* **2022**, *5* (6), 6913−6926.
(15) Payandeh, S.; Goonetilleke, D.; Bianchini, M.; Janek, J.; Brezesinski, T. Single versus poly-crystalline layered oxide cathode materials for solid-state battery applications - a short review article. *Curr. Opin. Electrochem.* **2022**, *31*, 100877.
(16) Zhao, Q.; Stalin, S.; Zi Zhao, C.; Archer, L. A. Designing solid-state electrolytes for safe, energy-dense batteries. *Nat. Rev. Mater.* **2020**, *5* (3), 229−252.
(17) Mangani, L. R.; Villevieille, C. Mechanical vs. chemical stability of sulphide-based solid-state batteries. Which one is the biggest challenge to tackle? Overview of solid-state batteries and hybrid solid state batteries. *J. Mater. Chem. A* **2020**, *8* (20), 10150−10167.
(18) Laiqiang, X.; Jiayang, L.; Shuai, H.; Luo, Z.; Wang, B.; Fang, S.; Zou, G.; Hou, H.; Peng, H.; Xiaobo, J. Recent advances of composite electrolytes for solid-state Li batteries. *J. Energy Chem.* **2022**, *67*, 524−548.
(19) Kwak, H.; Wang, S.; Park, J.; Liu, Y.; Kim, K. T.; Choi, Y.; Mo, Y.; Jung, Y. S. Emerging Halide Superionic Conductors for All-Solid-State Batteries: Design, Synthesis, and Practical Applications. *ACS Energy Lett.* **2022**, *7* (5), 1776−1805.
(20) Woolley, H. M.; Vargas-Barbosa, N. M. Hybrid solid electrolyte-liquid electrolyte systems for (almost) solid-state batteries: Why, how, and where to? *J. Mater. Chem. A* **2023**, *11* (11), 1083−1097.
(21) Huo, H.; Janek, J. Solid-state batteries: from'all-solid' to'almost-solid'. *Natl. Sci. Rev.* **2023**, *10* (6), 1−3.
(22) Lin, J.; Schaller, M.; Cherkashinin, G.; Indris, S.; Du, J.; Ritter, C.; Kondrakov, A.; Janek, J.; Brezesinski, T.; Strauss, F. Synthetic Tailoring of Ionic Conductivity in Multicationic Substituted, High-Entropy Lithium Argyrodite Solid Electrolytes. *Small* **2024**, *20*, 2306832.
(23) Lin, J.; Cherkashinin, G.; Schäfer, M.; Melinte, G.; Indris, S.; Kondrakov, A.; Janek, J.; Brezesinski, T.; Strauss, F. A High-Entropy Multicationic Substituted Lithium Argyrodite Superionic Solid Electrolyte. *ACS Mater. Lett.* **2022**, *4* (11), 2187−2194.
(24) Demuth, T.; Fuchs, T.; Walther, F.; Pokle, A.; Ahmed, S.; Malaki, M.; Beyer, A.; Janek, J.; Volz, K. Influence of the sintering temperature on LLZO-NCM cathode composites for solid-state batteries studied by transmission electron microscopy. *Matter* **2023**, *6* (7), 2324−2339.
(25) Janek, J.; Zeier, W. G. Challenges in speeding up solid-state battery development. *Nat. Energy* **2023**, *8* (3), 230−240.
(26) Xiao, Y.; Miara, L. J.; Wang, Y.; Ceder, G. Computational Screening of Cathode Coatings for Solid-State Batteries. *Joule* **2019**, *3* (5), 1252−1275.
(27) Lou, S.; Zhang, F.; Fu, C.; Chen, M.; Ma, Y.; Yin, G.; Wang, J. Interface Issues and Challenges in All-Solid-State Batteries: Lithium, Sodium, and Beyond. *Adv. Mater.* **2021**, *33* (6), 2000721.
(28) Liang, Y.; Liu, H.; Wang, G.; Wang, C.; Ni, Y.; Nan, C.-W.; Fan, L.-Z. Challenges, interface engineering, and processing strategies toward practical sulfide-based all-solid-state lithium batteries. *InfoMat* **2022**, *4* (5), No. e12292.
(29) Tong Zuo, T.; Rueß, R.; Pan, R.; Walther, F.; Rohnke, M.; Hori, S.; Kanno, R.; Schröder, D.; Janek, J. A mechanistic investigation of the Li10GeP2S12|LiNi1-x-yCoxMnyO2 interface stability in all-solid-state lithium batteries. *Nat. Commun.* **2021**, *12* (1), 6669.
(30) Li, X.; Ren, Z.; Norouzi Banis, M.; Deng, S.; Zhao, Y.; Sun, Q.; Wang, C.; Yang, X.; Li, W.; Liang, J.; Li, X.; Sun, Y.; Adair, K.; Li, R.; Hu, Y.; Sham, T.-K.; Huang, H.; Zhang, L.; Lu, S.; Luo, J.; Sun, X. Unravelling the Chemistry and Microstructure Evolution of a Cathodic Interface in Sulfide-Based All-Solid-State Li-Ion Batteries. *ACS Energy Lett.* **2019**, *4* (10), 2480−2488.
(31) Walther, F.; Randau, S.; Schneider, Y.; Sann, J.; Rohnke, M.; Richter, F. H.; Zeier, W. G.; Janek, J. Influence of Carbon Additives on the Decomposition Pathways in Cathodes of Lithium Thiophosphate-Based All-Solid-State Batteries. *Chem. Mater.* **2020**, *32* (14), 6123−6136.
(32) Auvergniot, J.; Cassel, A.; Ledeuil, J.-B.; Viallet, V.; Seznec, V.; Dedryvère, R. Interface Stability of Argyrodite Li6PS5Cl toward LiCoO2, LiNi1/3Co1/3Mn1/3O2, and LiMn2O4 in Bulk All-Solid-State Batteries. *Chem. Mater.* **2017**, *29* (9), 3883−3890.
(33) Walther, F.; Koerver, R.; Fuchs, T.; Ohno, S.; Sann, J.; Rohnke, M.; Zeier, W. G.; Janek, J. Visualization of the Interfacial Decomposition of Composite Cathodes in Argyrodite-Based All-Solid-State Batteries Using Time-of-Flight Secondary-Ion Mass Spectrometry. *Chem. Mater.* **2019**, *31* (10), 3745−3755.
(34) Visbal, H.; Aihara, Y.; Ito, S.; Watanabe, T.; Park, Y.; Doo, S. The effect of diamond-like carbon coating on LiNi0.8Co0.15Al0.05O2 particles for all solid-state lithium-ion batteries based on Li2S−P2S5 glass-ceramics. *J. Power Sources* **2016**, *314*, 85−92.
(35) Zuo, T.-T.; Walther, F.; Teo, J. H.; Rueß, R.; Wang, Y.; Rohnke, M.; Schröder, D.; Nazar, L. F.; Janek, J. Impact of the Chlorination of Lithium Argyrodites on the Electrolyte/Cathode Interface in Solid-State Batteries. *Angew. Chem., Int. Ed.* **2023**, *62* (7), No. e202213228.
(36) Kobayashi, S.; Watanabe, H.; Kato, T.; Mizuno, F.; Kuwabara, A. Atomic-Scale Observations of Oxygen Release Degradation in Sulfide-Based All-Solid-State Batteries with Layered Oxide Cathodes. *ACS Appl. Mater. Interfaces* **2022**, *14* (34), 39459−39466.
(37) Bartsch, T.; Strauss, F.; Hatsukade, T.; Schiele, A.; Kim, A.-Y.; Hartmann, P.; Janek, J.; Brezesinski, T. Gas Evolution in All-Solid-State Battery Cells. *ACS Energy Lett.* **2018**, *3* (10), 2539−2543.
(38) Strauss, F.; Teo, J. H.; Schiele, A.; Bartsch, T.; Hatsukade, T.; Hartmann, P.; Janek, J.; Brezesinski, T. Gas Evolution in Lithium-Ion Batteries: Solid versus Liquid Electrolyte. *ACS Appl. Mater. Interfaces* **2020**, *12* (18), 20462−20468.
(39) Conforto, G.; Ruess, R.; Schröder, D.; Trevisanello, E.; Fantin, R.; Richter, F. H.; Janek, J. Editors' Choice—Quantification of the Impact of Chemo-Mechanical Degradation on the Performance and Cycling Stability of NCM-Based Cathodes in Solid-State Li-Ion Batteries. *J. Electrochem. Soc.* **2021**, *168* (7), 70546.
(40) Morchhale, A.; Tang, Z.; Yu, C.; Farahati, R.; Kim, J.-H. Coating materials and processes for cathodes in sulfide-based all solid-state batteries. *Curr. Opin. Electrochem.* **2023**, *39*, 101251.
(41) Culver, S. P.; Koerver, R.; Zeier, W. G.; Janek, J. On the Functionality of Coatings for Cathode Active Materials in Thiophosphate-Based All-Solid-State Batteries. *Adv. Energy Mater.* **2019**, *9*, 1900626.
(42) Nakamura, T.; Amezawa, K.; Kulisch, J.; Zeier, W. G.; Janek, J. Guidelines for All-Solid-State Battery Design and Electrode Buffer

Layers Based on Chemical Potential Profile Calculation. *ACS Appl. Mater. Interfaces* **2019**, *11* (22), 19968−19976.
(43) Payandeh, S.; Strauss, F.; Mazilkin, A.; Kondrakov, A.; Brezesinski, T. Tailoring the LiNbO3 coating of Ni-rich cathode materials for stable and high-performance all-solid-state batteries. *Nano Res. Energy* **2022**, *1* (3), No. e9120016.
(44) Ma, Y.; Zhang, R.; Tang, Y.; Ma, Y.; Teo, J. H.; Diemant, T.; Goonetilleke, D.; Janek, J.; Bianchini, M.; Kondrakov, A.; Brezesinski, T. Single- to Few-Layer Nanoparticle Cathode Coating for Thiophosphate-Based All-Solid-State Batteries. *ACS Nano* **2022**, *16* (11), 18682−18694.
(45) Zhang, R.; Ma, Y.; Tang, Y.; Goonetilleke, D.; Diemant, T.; Janek, J.; Kondrakov, A.; Brezesinski, T. Conformal Li2HfO3/HfO2 Nanoparticle Coatings on Layered Ni-Rich Oxide Cathodes for Stabilizing Interfaces in All-Solid-State Batteries. *Chem. Mater.* **2023**, *35* (17), 6835−6844.
(46) Shi, B.-X.; Yusim, Y.; Sen, S.; Demuth, T.; Ruess, R.; Volz, K.; Henss, A.; Richter, F. H. Mitigating Contact Loss in Li6PS5Cl-Based Solid-State Batteries Using a Thin Cationic Polymer Coating on NCM. *Adv. Energy Mater.* **2023**, *13* (24), 2300310.
(47) Wang, J.; Zhao, S.; Zhang, A.; Zhuo, H.; Zhang, G.; Han, F.; Zhang, Y.; Tang, L.; Yang, R.; Wang, L.; et al. Halide-Coated Ni-Rich NCM Improves Cycling Stability in Sulfide All-Solid-State Batteries. *ACS Appl. Energy Mater.* **2023**, *6* (7), 3671−3681.
(48) Zuo, T.-T.; Walther, F.; Ahmed, S.; Rueß, R.; Hertle, J.; Mogwitz, B.; Volz, K.; Janek, J. Formation of an Artificial Cathode−Electrolyte Interphase to Suppress Interfacial Degradation of Ni-Rich Cathode Active Material with Sulfide Electrolytes for Solid-State Batteries. *ACS Energy Lett.* **2023**, *8* (3), 1322−1329.
(49) Moryson, Y.; Walther, F.; Sann, J.; Mogwitz, B.; Ahmed, S.; Burkhardt, S.; Chen, L.; Klar, P. J.; Volz, K.; Fearn, S.; Rohnke, M.; Janek, J. Analyzing Nanometer-Thin Cathode Particle Coatings for Lithium-Ion Batteries—The Example of TiO2 on NCM622. *ACS Appl. Energy Mater.* **2021**, *4* (7), 7168−7181.
(50) Teo, J. H.; Strauss, F.; Walther, F.; Ma, Y.; Payandeh, S.; Scherer, T.; Bianchini, M.; Janek, J.; Brezesinski, T. The interplay between (electro)chemical and (chemo)mechanical effects in the cycling performance of thiophosphate-based solid-state batteries. *Mater. Futures* **2022**, *1* (1), 15102.
(51) Hertle, J.; Walther, F.; Lombardo, T.; Kern, C.; Pavlovic, B.; Mogwitz, B.; Wu, X.; Schneider, H.; Rohnke, M.; Janek, J. Benchmarking of Coatings for Cathode Active Materials in Solid-State Batteries Using Surface Analysis and Reference Electrodes. *ACS Appl. Mater. Interfaces* **2024**, *16*, 9400−9413.
(52) Zhang, W.; Weber, D. A.; Weigand, H.; Arlt, T.; Manke, I.; Schröder, D.; Koerver, R.; Leichtweiss, T.; Hartmann, P.; Zeier, W. G.; Janek, J. Interfacial Processes and Influence of Composite Cathode Microstructure Controlling the Performance of All-Solid-State Lithium Batteries. *ACS Appl. Mater. Interfaces* **2017**, *9* (21), 17835−17845.
(53) Lombardo, T. *User-friendly Scripts for Experimental Battery Researachers*. https://github.com/teolombardo/User-friendly-scripts-for-experimental-battery-researchers. (Accessed 04 March 2025).
(54) Aktekin, B.; Sedykh, A. E.; Müller-Buschbaum, K.; Henss, A.; Janek, J. The Formation of Residual Lithium Compounds on Ni-Rich NCM Oxides: Their Impact on the Electrochemical Performance of Sulfide-Based ASSBs. *Adv. Funct. Mater.* **2024**, *34*, 2313252.
(55) Wood, K. N.; Teeter, G. XPS on Li-Battery-Related Compounds: Analysis of Inorganic SEI Phases and a Methodology for Charge Correction. *ACS Appl. Energy Mater.* **2018**, *1* (9), 4493−4504.
(56) Nagao, K.; Hayashi, A.; Deguchi, M.; Tsukasaki, H.; Mori, S.; Tatsumisago, M. Amorphous LiCoO2-Li2SO4 active materials: Potential positive electrodes for bulk-type all-oxide solid-state lithium batteries with high energy density. *J. Power Sources* **2017**, *348*, 1−8.
(57) Nikam, R. D.; Kwak, M.; Lee, J.; Rajput, K. G.; Banerjee, W.; Hwang, H. Near ideal synaptic functionalities in Li ion synaptic transistor using Li3POxSex electrolyte with high ionic conductivity. *Sci. Rep.* **2019**, *9* (1), 18883.
(58) Ahmed, S.; Pokle, A.; Schweidler, S.; Beyer, A.; Bianchini, M.; Walther, F.; Mazilkin, A.; Hartmann, P.; Brezesinski, T.; Janek, J.; Volz, K. The Role of Intragranular Nanopores in Capacity Fade of Nickel-Rich Layered Li(Ni1-x-yCoxMny)O2 Cathode Materials. *ACS Nano* **2019**, *13* (9), 10694−10704.
(59) Hidde, H. B. Low-Energy Ion Scattering. In *Characterization of Materials*; John Wiley & Sons, 2012, pp. 1−23. DOI: .
(60) Koerver, R.; Walther, F.; Aygün, I.; Sann, J.; Dietrich, C.; Zeier, W. G.; Janek, J. Redox-active cathode interphases in solid-state batteries. *J. Mater. Chem. A* **2017**, *5* (43), 22750−22760.
(61) Karger, L.; Nunes, B. N.; Yusim, Y.; Mazilkin, A.; Zhang, R.; Zhao, W.; Henss, A.; Kondrakov, A.; Janek, J.; Brezesinski, T. Protective Nanosheet Coatings for Thiophosphate-Based All-Solid-State Batteries. *Adv. Mater. Interfaces* **2024**, *11* (14), 2301067.
(62) Wang, S.; Tang, M.; Zhang, Q.; Li, B.; Ohno, S.; Walther, F.; Pan, R.; Xu, X.; Xin, C.; Zhang, W.; Li, L.; Shen, Y.; Richter, F. H.; Janek, J.; Nan, C.-W. Lithium Argyrodite as Solid Electrolyte and Cathode Precursor for Solid-State Batteries with Long Cycle Life. *Adv. Energy Mater.* **2021**, *11* (31), 2101370.
(63) Schwietert, T. K.; Arszelewska, V. A.; Wang, C.; Yu, C.; Vasileiadis, A.; Klerk, N. J. J.; Hageman, J.; Hupfer, T.; Kerkamm, I.; Xu, Y.; et al. Clarifying the relationship between redox activity and electrochemical stability in solid electrolytes. *Nat. Mater.* **2020**, *19* (4), 428−435.
(64) Pokle, A.; Ahmed, S.; Schweidler, S.; Bianchini, M.; Brezesinski, T.; Beyer, A.; Janek, J.; Volz, K. In Situ Monitoring of Thermally Induced Effects in Nickel-Rich Layered Oxide Cathode Materials at the Atomic Level. *ACS Appl. Mater. Interfaces* **2020**, *12* (51), 57047−57054.

https://doi.org/10.1021/acs.chemmater.4c03086
Chem. Mater. 2025, 37, 2192−2203